J. Fluid Mech. (1991), *vol.* 225, *pp.* 1–20
Printed in Great Britain

The spatial structure and statistical properties of homogeneous turbulence

By A. VINCENT AND M. MENEGUZZI
CERFACS, 42 av. G. Coriolis, 31000 Toulouse, France

(Received 15 February 1990 and in revised form 17 September 1990)

A direct numerical simulation at resolution 240^3 is used to obtain a statistically stationary three-dimensional homogeneous and isotropic turbulent field at a Reynolds number around 1000 ($R_\lambda \approx 150$). The energy spectrum displays an inertial subrange. The velocity derivative distribution, known to be strongly non-Gaussian, is found to be close to, but not, exponential. The nth-order moments of this distribution, as well as the velocity structure functions, do not scale with n as predicted by intermittency models. Visualization of the flow confirms the previous finding that the strongest vorticity is organized in very elongated thin tubes. The width of these tubes is of the order of a few dissipation scales, while their length can reach the integral scale of the flow.

1. Introduction

Understanding the structure in space of a turbulent flow, as well as its statistical properties, remains a challenge both for the experimentalist and the theoretician. In recent years, direct simulation, i.e. resolution of the basic fluid dynamics equations using the most powerful computers, has proved to be a valuable additional tool for the study of fully developed turbulence. For the range of parameters in which they are feasible, the direct simulations allow measurement of many quantities unaccessible in the laboratory. Also, visualization of the small-scale structures of the flow is in principle easier. High-resolution simulations in two space dimensions at Reynolds numbers of several thousands or more are now standard, and have revealed new and important properties of two-dimensional turbulence (Basdevant *et al.* 1981; McWilliams 1984; Herring & McWilliams 1985; Brachet *et al.* 1983; Benzi, Patarnello & Santangelo 1987). Early attempts at direct solution of the three-dimensional Navier–Stokes equation were restricted to modest Reynolds numbers (Orszag & Patterson 1972; Siggia & Patterson 1978; Siggia 1981). They have allowed a study of the dissipation-scale properties of a turbulent flow. It now becomes feasible, on computers of the latest generation, to reach Reynolds numbers at which an inertial subrange of the energy spectrum exists (Kerr 1985; Yamamoto & Hosokawa 1988; She, Jackson & Orszag 1988, 1990). The object of the present paper is to study a more extended inertial subrange.

Several questions were raised by the results from the above authors. For instance, these simulations have revealed (Siggia 1981) that the vorticity field is organized in very long and thin tubes, but one did not know whether these are purely dissipation-scale structures or they extend to larger scales. Another feature of turbulent flow found in the calculations of Kerr (1985) is the independence of the velocity derivatives skewness of the Reynolds number, contrary to predictions of the intermittency models. The scaling of fourth-order moments with Reynolds number found by Kerr is also at variance with these models. It would be interesting to know whether this is still true at higher Reynolds numbers. It was also found in these calculations that the eigenvectors of the strain tensor correlate with vorticity. An explanation of the observed correlation is proposed in Ashurst *et al.* (1987), but a more detailed analysis seems required to verify it.

In the following section, we present our calculations. In §§3 and 4, we give the results on statistical properties of the flow, and in §5 we describe the structure of the flow which emerges from our three-dimensional visualizations.

2. The calculation

We solve the Navier–Stokes equation for incompressible fluids in rotational form:

$$\frac{\partial \boldsymbol{v}}{\partial t} = \boldsymbol{v} \times \boldsymbol{\omega} - \boldsymbol{\nabla}(p + \tfrac{1}{2}v^2) + \nu \nabla^2 \boldsymbol{v} + \boldsymbol{f}, \tag{1}$$

with the continuity equation

$$\boldsymbol{\nabla} \cdot \boldsymbol{v} = 0.$$

Here $\boldsymbol{v}$ is the velocity field, $\boldsymbol{\omega} = \boldsymbol{\nabla} \times \boldsymbol{v}$ the vorticity, p the pressure, ν the kinematic viscosity and $\boldsymbol{f}$ a force field. Since we are interested in (statistically) homogeneous turbulent flows, we take periodic boundary conditions in all directions, with period 2π. In Fourier space the two equations can be combined to give

$$\frac{\partial \boldsymbol{v}_k}{\partial t} = \boldsymbol{P}(\boldsymbol{k}) \cdot (\boldsymbol{v} \times \boldsymbol{\omega})_k - \nu k^2 \boldsymbol{v}_k + \boldsymbol{f}_k, \tag{2}$$

where the tensor $\boldsymbol{P}$ is the projector on the space of solenoidal fields, defined as

$$P_{ij}(\boldsymbol{k}) = \delta_{ij} - \frac{k_i k_j}{k^2}.$$

A pseudospectral method is used to compute the right-hand side of this equation (see Gottlieb & Orszag 1977), i.e. aliasing is not removed. Removing it would increase the cost of the calculation by a factor ≈ 2. To check that this was not necessary, we have redone part of our calculation (for several turnover times) with aliasing removed by the method outlined in Patterson & Orszag (1971), and we did not find any significant difference in the results. The importance of aliasing effects in pseudospectral methods is discussed in Orszag (1972). The time marching is done using a second-order finite-difference scheme. An Adams–Bashforth scheme is used for the nonlinear term while the dissipative term is integrated exactly. The resulting numerical scheme is

$$\frac{\boldsymbol{v}_k^{n+1} - \boldsymbol{v}_k^n \,\mathrm{e}^{-\nu k^2 \delta t}}{\delta t} = \boldsymbol{P}(\boldsymbol{k}) \cdot [\tfrac{3}{2}(\boldsymbol{v} \times \boldsymbol{\omega})_k^n \,\mathrm{e}^{-\nu k^2 \delta t} - \tfrac{1}{2}(\boldsymbol{v} \times \boldsymbol{\omega})_k^{n-1} \,\mathrm{e}^{-2\nu k^2 \delta t} + \boldsymbol{f}_k^n \,\mathrm{e}^{-\nu k^2 \delta t}].$$

To start (or restart) the calculation, we use a second-order Runge–Kutta scheme.

The simplest way to force the flow in this geometry would be to take as a force field a white noise in time. This would allow us to control the energy injection rate, which in this case would be $\langle f^2 \rangle$. However, introducing some randomness externally through the forcing would prevent us from asking questions about the intrinsic chaotic behaviour of the flow, for instance by studying time series of the velocity or its derivatives at a given point. We therefore chose to force the field in a deterministic way, as was done by Kerr (1985). All Fourier modes with wavenumber components equal to 1 or 0 are forced with a constant amplitude $\boldsymbol{f}$ independent of $\boldsymbol{k}$ (the components of $\boldsymbol{k}$ take only integer values, since the space period is 2π). This results in large fluctuations of the energy injection rate $\epsilon_i = \langle \boldsymbol{f} \cdot \boldsymbol{v} \rangle$. Owing to these fluctuations and also to the discretization, one can only hope to reach a steady-state regime in the sense that the mean kinetic energy density fluctuates in time around a constant value.

The calculation presented here was done with 240^3 Fourier components, and a viscosity of 10^{-3}. One time-step takes 12 s on a Cray-2, using the four processors. Integration over one turnover time (defined below) takes of the order of 4 h of Cray-2. The average speed-up obtained by using four processors instead of one is 2.5, since we never run in dedicated mode.

To estimate the degree of isotropy of the flow, we use the same method as Curry *et al.* (1984). For each wavenumber $\boldsymbol{k}$, we define two unit vectors $\boldsymbol{e}_1(\boldsymbol{k})$ and $\boldsymbol{e}_2(\boldsymbol{k})$, which, with $\boldsymbol{k}$, form an orthogonal reference frame. Since $\boldsymbol{k} \cdot \boldsymbol{v} = 0$, each Fourier mode $\boldsymbol{v}(\boldsymbol{k})$ is defined by its two components in this frame $v_1(\boldsymbol{k})$ and $v_2(\boldsymbol{k})$. We define the isotropy I as

$$I = \left[\frac{\langle |v_1|^2 \rangle}{\langle |v_2|^2 \rangle}\right]^{\frac{1}{2}}.$$

In the calculations presented here, I fluctuates by a few percent around 0.95. Therefore, our flow is close to statistically isotropic.

Let us recall the definition of some characteristic quantities to be used in the following. These characteristic lengths are used: the integral scale

$$l_0 = \frac{\int_0^\infty k^{-1} E(k)\, \mathrm{d}k}{\int_0^\infty E(k)\, \mathrm{d}k},$$

the Taylor microscale

$$\lambda = \left[\frac{\int_0^\infty E(k)\, \mathrm{d}k}{\int_0^\infty k^2 E(k)\, \mathrm{d}k}\right]^{\frac{1}{2}},$$

and the Kolmogorov dissipation scale

$$l_D = \left(\frac{\nu^3}{\epsilon}\right)^{\frac{1}{4}},$$

where ϵ is the mean energy dissipation rate per unit mass. The two characteristic timescales of homogeneous turbulence are the eddy turnover time

$$\tau_0 = l_0 / v_0,$$

where v_0 is the root-mean-square velocity, and the dissipation time

$$\tau_\nu = l_0^2 / \nu.$$

With these quantities one can define two Reynolds numbers: the integral-scale Reynolds number $R = v_0 l_0 / \nu$, and the Taylor-microscale Reynolds number $R_\lambda = \lambda v_0 / \nu$.

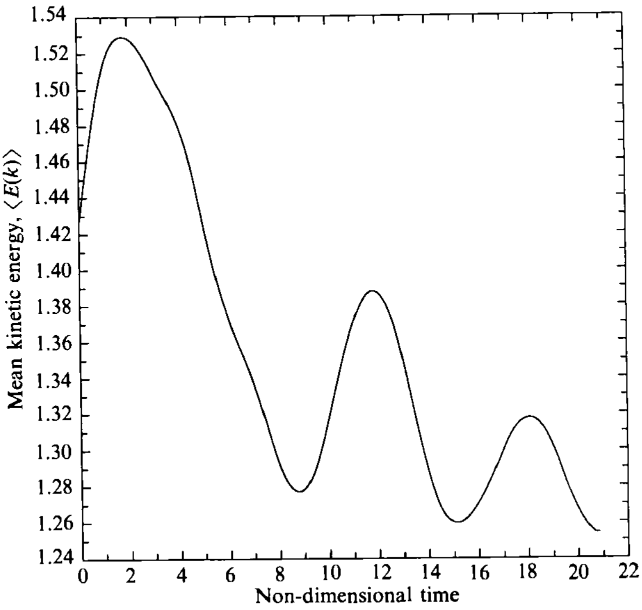

FIGURE 1. Mean kinetic energy per unit mass versus time. The turnover time is 0.35.

3. The spectra of the flow

After integration over a few tens of turnover times we obtain a statistically stationary regime in the above sense. Figure 1 shows the mean kinetic energy per unit mass $\langle \frac{1}{2}v^2 \rangle$ versus time. Our time unit is such that the large-eddy turnover time is 0.35. The total duration of our calculation is 60 turnover times. Only the second half of this time was used in our analysis, because it seems closer to a statistically steady state. The energy spectrum $E(k)$ at a given time is defined as

$$E(k) = \frac{1}{2} \sum_{k-\frac{1}{2} < |\boldsymbol{k}| \leqslant k+\frac{1}{2}} |\boldsymbol{v}_k|^2.$$

It is shown in figure 2 at time 14. A power-law range can be seen for $k < 25$, with an exponent a little larger than $-\frac{5}{3}$. The dashed line shows the same spectrum multiplied by $k^{\frac{5}{3}}$. The fact that this is an inertial range is confirmed by inspection of the energy flux spectrum, shown in figure 3. The energy flux $\Phi(k)$ is defined as

$$\Phi(k) = \int_k^\infty T(k)\,\mathrm{d}k, \tag{3}$$

where $T(k)$ is the energy transfer, which appears in the energy equation

$$\frac{\mathrm{d}E}{\mathrm{d}t}(k) = F(k) + T(k) - 2\nu k^2 E(k) \tag{4}$$

($F(k)$ is the energy injection spectrum). In other words, $\Phi(k)$ is the rate of energy transferred per unit mass by all modes with $k' < k$ to modes with $k' > k$. From equation (2), the energy transfer is

$$T(k) = \int \boldsymbol{v}_k \cdot \boldsymbol{P}(\boldsymbol{k}) \cdot (\boldsymbol{v} \times \boldsymbol{\omega})_k \,\mathrm{d}\Omega, \tag{5}$$

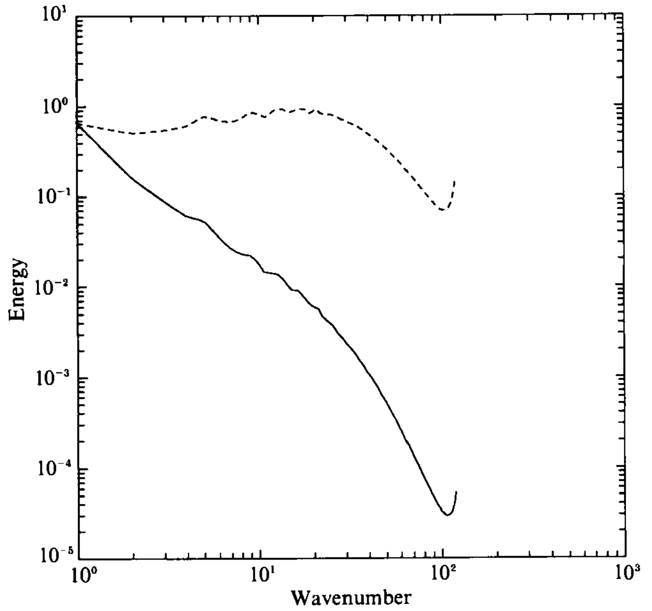

FIGURE 2. Energy spectrum at a given time (continuous curve). Same energy spectrum multiplied by $k^{\frac{5}{3}}$ (dashed curve).

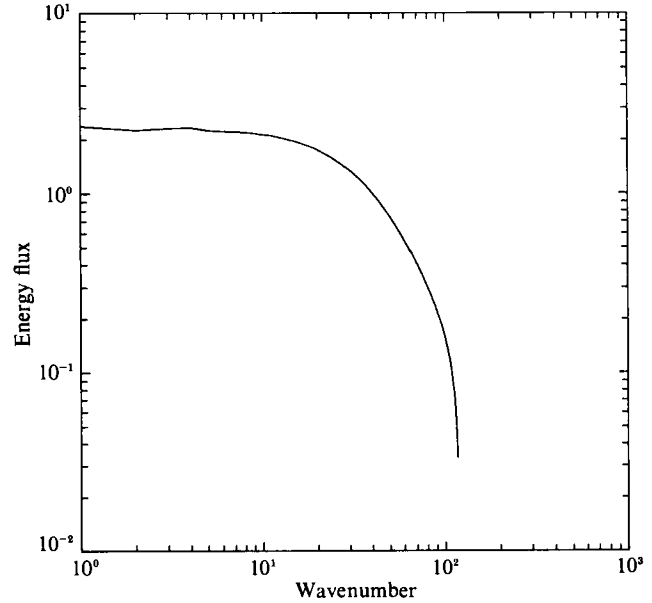

FIGURE 3. Energy flux corresponding to the spectrum of figure 2.

where the integration is over the angles in Fourier space. By definition, the energy flux is constant in the inertial range, which is seen in figure 3 to occupy a little more than one decade in wavenumber space. The small increase in the energy spectrum at the highest wavenumbers is due to a lack of resolution for our Reynolds number $R \approx 1000$ ($R_\lambda \approx 150$). Note that this spurious tail in the spectrum does not disappear when aliasing is removed, but does only when the viscosity is increased by a large

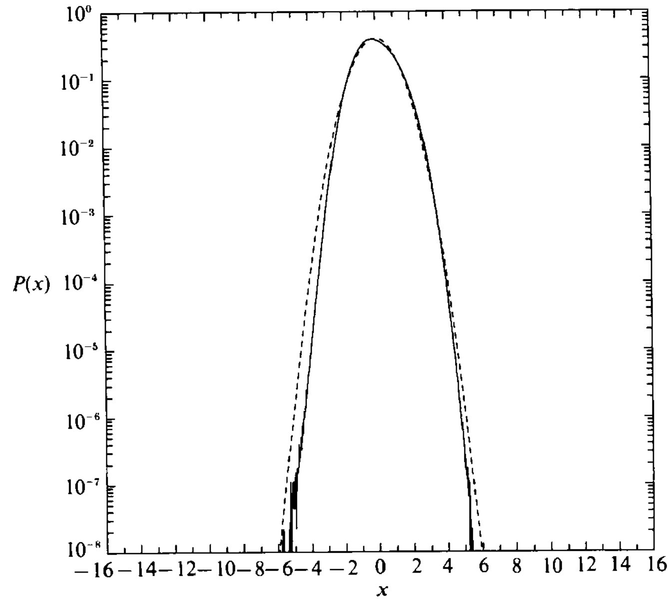

FIGURE 4. Probability distribution of a velocity component v_x, normalized so that $\sigma = 1$, shown together with a Gaussian distribution (dashed line).

factor. This should certainly be done in a simulation devoted to the study of the dissipation subrange. But in the present work, we wanted to focus on the inertial subrange.

The energy spectrum does not vary significantly during the second half of our integration. By fitting this spectrum with the Kolmogorov form

$$E(k) = C_K \epsilon^{\frac{2}{3}} k^{-\frac{5}{3}}, \tag{6}$$

we obtain a value of 2 for the 'Kolmogorov constant' C_K, which does not vary by more than 3% in the statistically steady-state period. This value of C_K is a little larger than the experimental value ≈ 1.5 (see Monin & Yaglom 1975 for references). Kerr (1990) has also found a larger value in numerical experiments at $R_\lambda = 83$.

4. The statistical distribution of v and its derivatives

It is generally assumed that turbulent flows are ergodic, and experimentalists use time distributions of a velocity component v_i or its derivatives $\partial_i v_j$ at a given space location to obtain probability distributions. Our time series are too short to apply the same method to our results. It seems more efficient to use space distributions, for which we have $\approx 1.4 \times 10^7$ grid point values at each time. Using approximately 100 different times, we reach a total of $\approx 1.4 \times 10^9$ values. The resulting statistical distribution of v_x is shown in figure 4, after being normalized so that $\sigma^2 = \langle v_x^2 \rangle = 1$. It is compared to a Gaussian distribution, shown with a dashed line. The distribution we obtain is close to Gaussian, in agreement with what is known from experimental data (see Monin & Yaglom 1975 for a review), and from previous simulations (Schumann & Patterson 1978).

Figure 5 shows the distribution of $\partial_x v_x$, known from experiments to be strongly non-Gaussian. Also shown is a Gaussian, again normalized so that $\sigma = 1$. It is seen

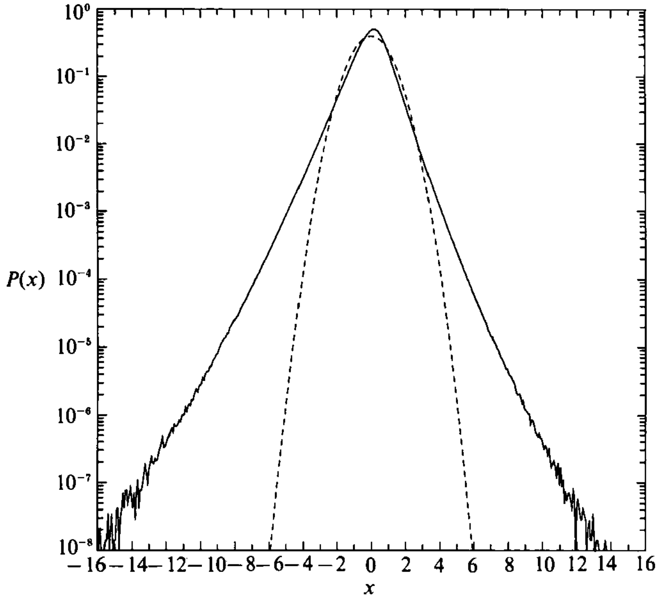

FIGURE 5. Probability distribution of $\partial v_x/\partial x$ normalized so that $\sigma = 1$, shown together with a Gaussian distribution (dashed line).

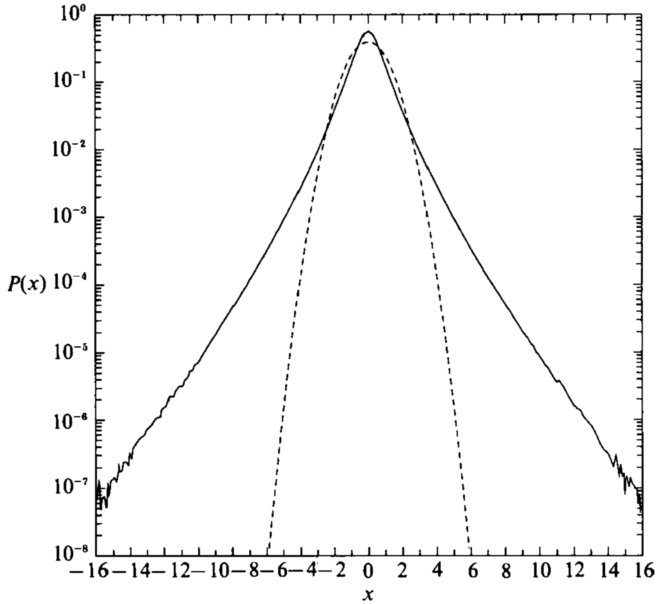

FIGURE 6. Probability distribution of $\partial v_x/\partial y$ normalized so that $\sigma = 1$, shown together with a Gaussian distribution (dashed line).

that the distribution we obtain is closer to an exponential than to a Gaussian, but our statistical sample allows one to see a departure from an exponential law. The wings are indeed not straight lines in this linear-logarithmic plot. The distribution is more intermittent than an exponential distribution. Recently, Castaing, Gagne & Hopfinger (1990) have reported similar distributions from experimental data, and

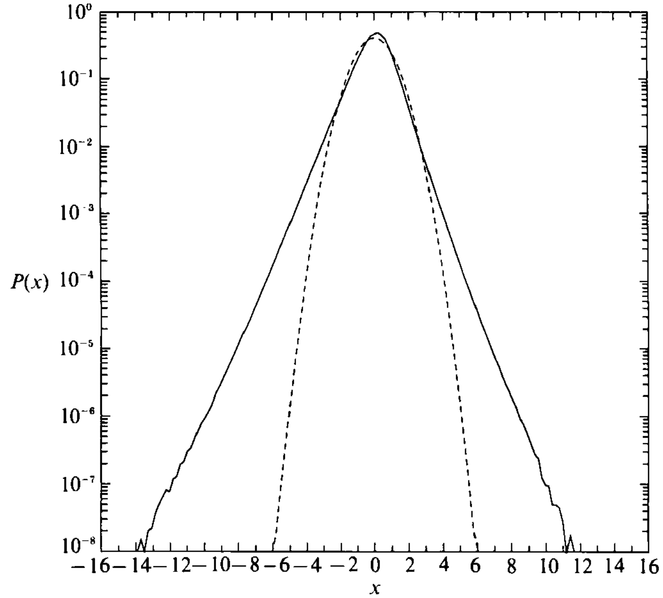

FIGURE 7. Probability distribution of $\delta v_x(r) = v_x(x+r) - v_x(x)$ for $r = 0.05$ (a dissipation scale), normalized so that $\sigma = 1$, shown together with a Gaussian distribution (dashed line).

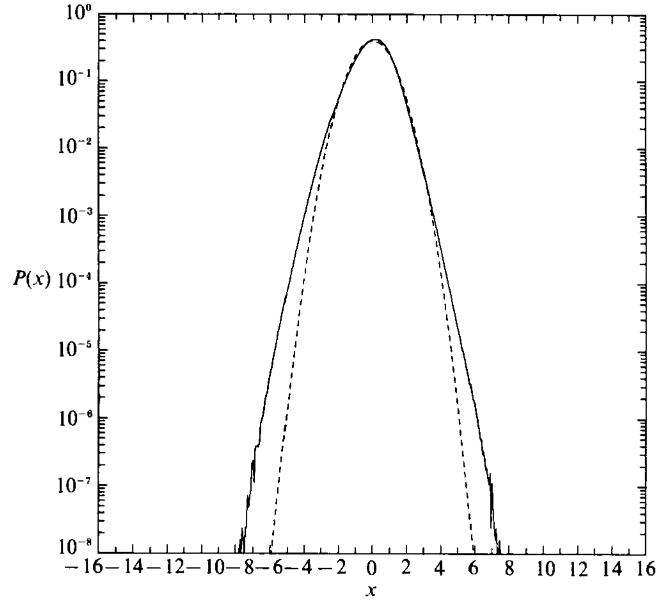

FIGURE 8. Same as figure 7 with $r = 0.39$, a typical inertial-range scale.

Kraichnan (1990) has obtained them from a closure model. This curvature is even more pronounced for the distribution of lateral derivatives $\partial_y v_x$, shown in figure 6. It is known (see for instance She *et al.* 1988) that the large wings of these distributions are due mainly to small-scale velocity fluctuations. It is therefore important to check whether the non-exponential wings could come from a lack of resolution of our calculation. We have recomputed the distribution with a velocity field obtained by filtering the highest wavenumbers so that the non-physical tail (figure 2) disappears in its energy spectrum. The wing curvature in plots analogous to the one in figures 5 and 6 was still present.

The moments of the distribution of $\partial_x v_x$,

$$S_n = \frac{\langle(\partial_x v_x)^n\rangle}{\langle(\partial_x v_x)^2\rangle^{n/2}}, \tag{7}$$

can be computed from the distribution shown in figure 5. We find a value of the skewness $S_3 = -0.5$. This agrees exactly with the value found by Kerr (1985) at $R_\lambda < 80$, and confirms the tendency he found for S_3 to be independent of the Reynolds number, a result at variance with intermittency models (Kolmogorov 1962; Oboukhov 1962; Novikov & Stewart 1964; Frisch, Sulem & Nelkin 1978). For the flatness factor S_4, we find 5.9, a value which fits the curve given by Kerr (1985) from his points for $R_\lambda < 80$, and which has the analytical form $S_4 \sim R_\lambda^{0.18}$. The values we find for S_5 and S_6 are respectively 9 and 90. The lateral derivatives $\partial_y v_x$ and $\partial_z v_x$ do not have the same skewness and flatness. The skewness of the $\partial_y v_x$ distribution is expected to be zero for a statistically isotropic field (see Monin & Yaglom 1975). It can be seen from figure 6 that the $\partial_y v_x$ distribution is much more symmetric than that of $\partial_x v_x$ (figure 5), and this results in smaller odd-order moments. However, our turbulent field is close to, but not exactly, isotropic, and we find a value of -0.04 for this skewness. Concerning the flatness of $\partial_y v_x$, it was shown by Siggia (1981) that for a statistically isotropic flow there are only four independent fourth-order rotational invariants, and flatness factors can be expressed in terms of those. Therefore, the flatnesses of $\partial_x v_x$ and $\partial_y v_x$ are not necessarily equal. We find a value of 8 for the latter, larger than the 5.9 value of the former.

We have also computed the distribution of velocity differences,

$$\delta v_x(r) = v_x(\boldsymbol{x}+\boldsymbol{r}, t) - v_x(\boldsymbol{x}),$$

which depend only on r for homogeneous isotropic turbulence. Figure 7 shows the distribution of δv_x for $r = 0.05$, a value typical of the dissipation-range scales, while figure 8 shows the same for $r = 0.39$, a value which belongs to the inertial range. These distributions seem to display exponential wings. They are similar to the experimental distributions found by Anselmet *et al.* (1984) and Van Atta & Chen (1970). For the largest values of r, the distribution of δv_x is Gaussian. Therefore, when r goes from 0 to values > 1, the δv_x distribution changes continuously from a function similar to the $\partial_x v_x$ distribution (figure 5) to a Gaussian. For intermediate values of r the wings look exponential (figure 8). Our results do not rule out the possibility that they are indeed exponential for r in the inertial range. From these distributions, one can compute the velocity structure functions, defined as

$$F_n(r) = \langle[\delta v_x(r)]^n\rangle, \tag{8}$$

or the dimensionless structure functions, given by

$$f_n(r) = \frac{\langle[\delta v_x(r)]^n\rangle}{\langle[\delta v_x(r)]^2\rangle^{n/2}}. \tag{9}$$

To estimate the maximum value of n for which this calculation can be done accurately, we use a method analogous to the one used by Anselmet *et al.* The structure functions are computed in two different ways: once with the distributions as they are, and a second time with a distribution obtained by extending the exponential wings to plus and minus infinity. This gives a rough estimate of the error

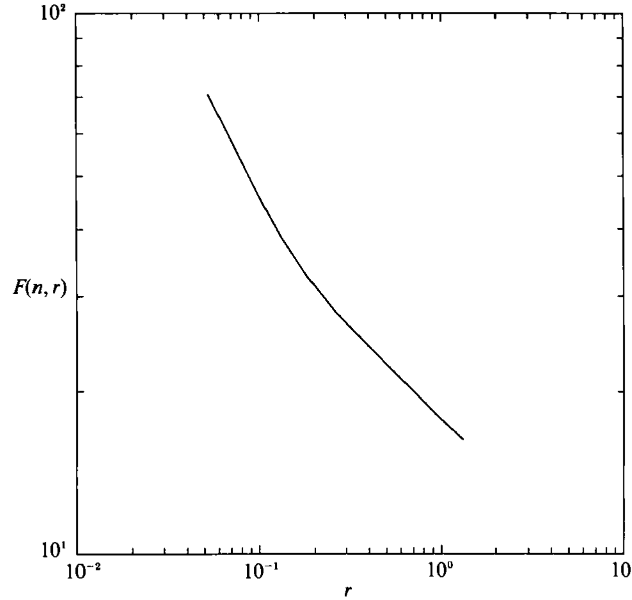

FIGURE 9. Structure function of order 6, $F_6(r) = \langle[\delta v_x(r)]^6\rangle$ as a function of r. Note the power-law form for r in the inertial range ($r > 0.2$).

due to our limited knowledge of these wings. For r in the inertial range, the two computed values agree to within a few percent for $n < 20$ and within 40% for $n < 30$. A second test done by Anselmet *et al.* was to plot the structure function values versus sample size and check their convergence when the sample increases. We have done this and found convergence for structure functions of order < 30, with our sample of 1.4×10^9 values. Figure 9 shows an example of structure function $f_6(r)$. In the inertial-range values of r ($r > 0.2$) this function is indeed a power law. This is typically the case for all even values of n. Note that the structure functions are much more accurately computed for even values of n than for odd values, since the integrand is definite positive in the former case while in the latter, the positive and negative δv_x parts of the integral are of opposite sign. We therefore rely on the even structure functions in the following.

Intermittency models of turbulence predict power-law forms of the structure functions for r in the inertial range

$$F_n(r) \sim r^{\zeta_n} \tag{10}$$

with ζ_n given by

$$\zeta_n = \tfrac{1}{3}n - \tfrac{1}{18}\mu n(n-3) \tag{11}$$

in the case of the Kolmogorov–Oboukov log-normal (LN) model, and

$$\zeta_n = \tfrac{1}{3}n - \tfrac{1}{3}\mu(n-3) \tag{12}$$

in the case of the β-model (Frisch *et al.* 1978; Novikov & Stewart 1964). Both predictions coincide for $n = 6$, for which $\zeta_6 = 2-\mu$. The dimensionless structure function $f_n(r)$ also has a power law form r^{ξ_n} with $\xi_n = \zeta_n - \tfrac{1}{2}n\zeta_2$. Figure 10 shows ζ_n as a function of n, and compares it with the predictions of the LN model, the β-model and the Kolmogorov (1941, 1962) theory ($\mu = 0, \zeta_n = \tfrac{1}{3}n$). It is seen that none of the predictions fits our results. This figure is similar to figure 14 of Anselmet *et al.* (1984), who drew the same conclusion from their experimental data. Note that their

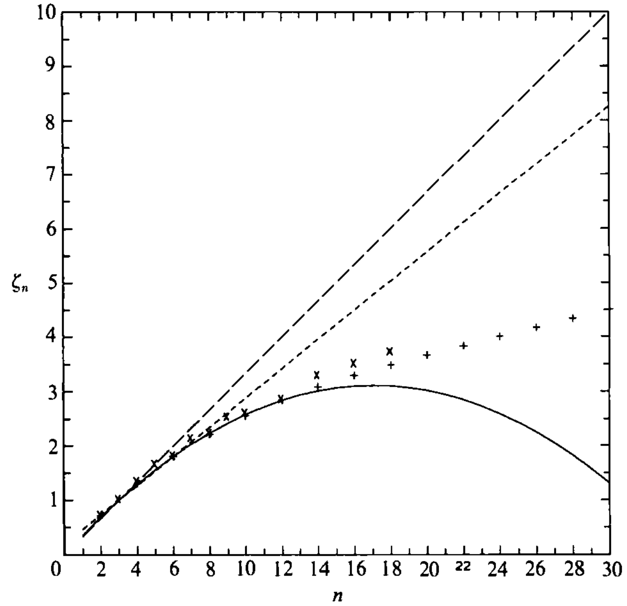

FIGURE 10. Power-law exponent ζ_n of the structure functions $F_n(r) \sim r^{\zeta_n}$ as a function of n. ---, prediction of the Kolmogorov (1941) theory; ----, β-model; ——, Kolmogorov (1962) model; +, values from our simulation; ×, experimental values of Anselmet *et al.* (1984) for $R_\lambda = 852$.

Reynolds number $R_\lambda > 500$ is much larger than ours. Both the experimental data values and our results are closer to the LN than to the β-model curve. However, we do not observe any maximum of ζ_n followed by a decrease, as given by equation (11) for large n. More recently, a 'multifractal model' was proposed by Parisi & Frisch (1984). This model does not make a firm prediction of the shape of ζ_n, but states that ζ_n is the Legendre transform of $D(h)$, the fractal dimension of the set of singularities of v with exponent h. (See Bacry *et al.* 1990.) A test of this model would be a proof that these sets are indeed fractal. We did not attempt to do this in the present work, since it would require a knowledge of the function ζ_n with very high accuracy, particularly at the highest and lowest n.

The value we find for $\mu = 2 - \zeta_6$ is 0.20, in agreement with the value found in the laboratory by Anselmet *et al.*, also using ζ_6. In the above models, the parameter μ is identified with the power-law exponent of the dissipation-rate correlation

$$\langle \epsilon(\boldsymbol{x}+\boldsymbol{r})\,\epsilon(\boldsymbol{x})\rangle \sim \left(\frac{l_0}{r}\right)^{\mu}. \tag{13}$$

We can obtain μ directly through (13). The value of this correlation versus r is given in figure 11. The value of μ inferred from the slope in the inertial range ($r > 0.2$) is not very accurately determined, and approximately equal to 0.13, a value lower than the one obtained above. Note that the coefficient μ found using (11) or (12) with $n = 6$ is a pure inertial-range quantity, while this is not so for the exponent appearing in (13), even for r in the inertial range (Kraichnan 1974). It is therefore possible that they are different.

To check the validity of our statistical analysis, we have divided our sample into two equal sets and redone the analysis for each set. The probability distributions look very similar. The exponent μ in (11) is close to 0.25 in the first sample, and to 0.15

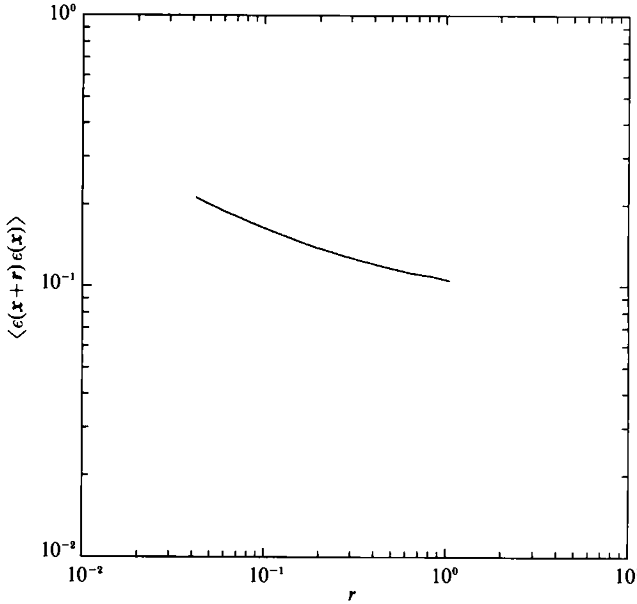

FIGURE 11. Energy dissipation correlation $\langle \epsilon(x+r)\epsilon(x)\rangle$ versus r at the end of our calculation.

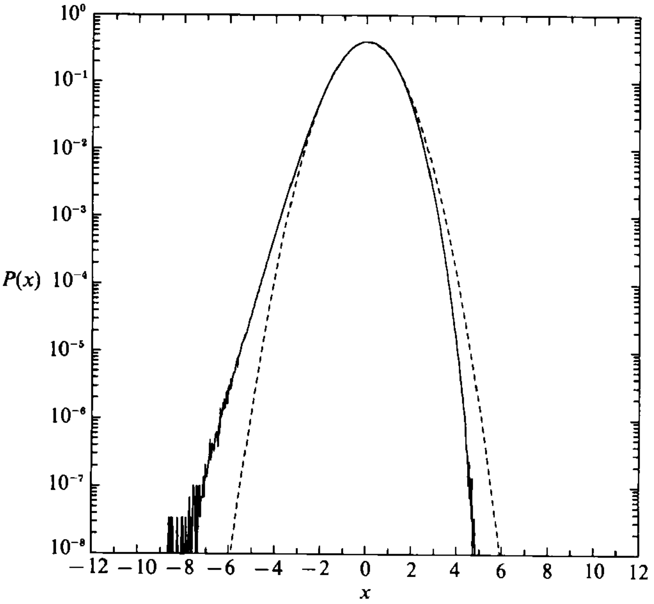

FIGURE 12. Probability distribution of $\log \epsilon(x)$, where ϵ is the energy dissipation per unit mass, normalized so that $\sigma = 1$, shown together with a Gaussian distribution (dashed line).

in the second. This is probably a consequence of the large fluctuations produced by our forcing.

An independent test of the LN model is a direct verification of Kolmogorov's third hypothesis, which states that the distribution of ϵ, the energy dissipation rate per unit mass, is log-normal (Kolmogorov 1962). We have plotted in figure 12 the distribution of $\log \epsilon$, together with a properly normalized Gaussian (dashed line). One

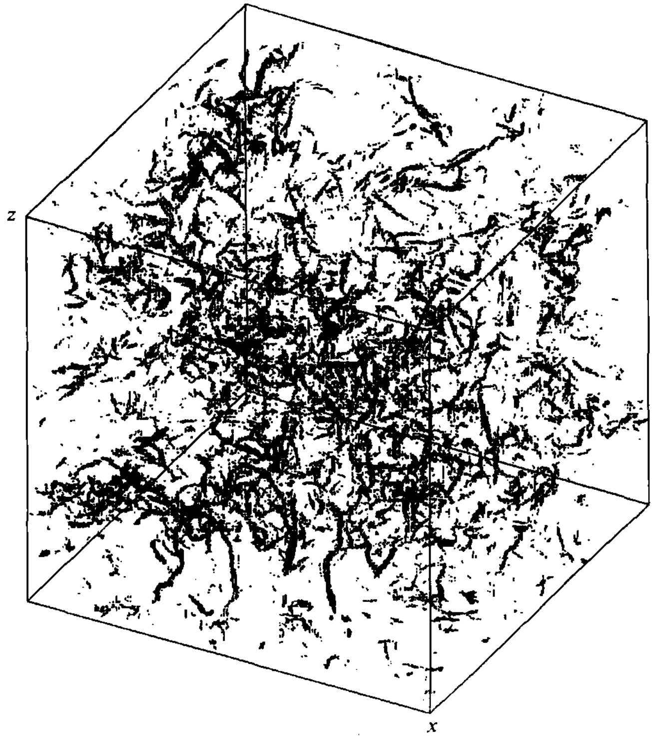

FIGURE 13. View of the vorticity field, represented by a vector of length proportional to the vorticity amplitude at each grid point. Only vectors larger than a given threshold value are shown.

can see that the distribution is definitely not normal, although it is close to normal for small fluctuations of log ϵ.

5. The spatial structure of the flow

Figure 13 shows a three-dimensional picture of the vorticity field. The vorticity at each grid point is represented by a vector, here so small that individual vectors can hardly be seen. Vectors are only plotted if their modulus is larger than a given threshold. By varying this threshold and rotating the figure on a graphic workstation screen we can explore the structure of the field in detail. One can see that the vorticity is organized in thin elongated tubes, as previously reported by Siggia (1981), Kerr (1985), She *et al.* (1990). Figure 14 shows the effect of lowering the threshold, and therefore letting smaller amplitude vorticity vectors appear. The length of these tubes seems to be of order 1, i.e. of the same order as the integral scale (the cube size is 2π). Their thickness is of the order of a few dissipation scales, here a few grid points. This is confirmed by a more detailed analysis. Figure 15 shows a cut through a typical vorticity tube, and shows clearly that its characteristic thickness is a few grid points. The dissipation scale l_D, in our simulation, is of the order of the mesh size, while the Taylor microscale is approximately ten mush sizes. Therefore, the characteristic tube thickness seems to be intermediate between these two lengths. Figure 16 shows a detailed view of a vorticity tube. It displays a sub-cube one sixth the size of the complete one, with 40 grid points on each side. Similar

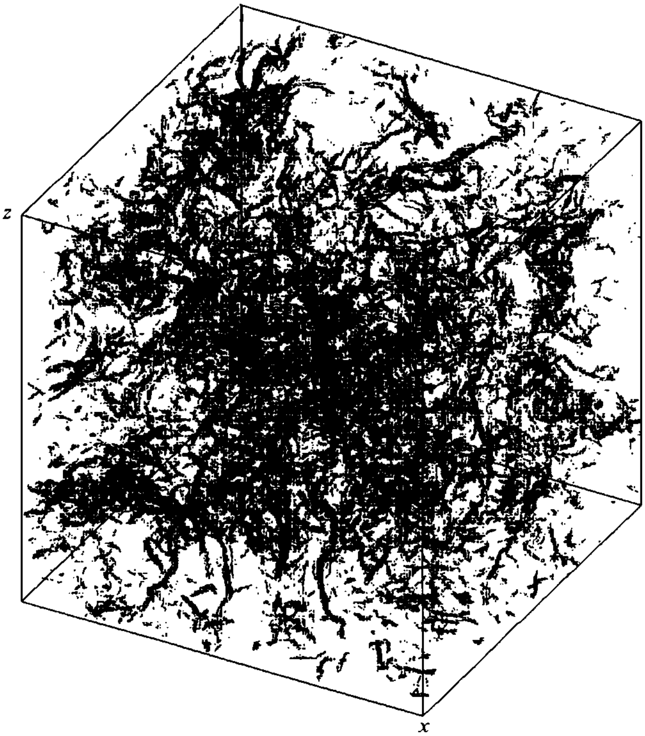

FIGURE 14. Same as in figure 13, but with a lower threshold value, and therefore more vectors represented.

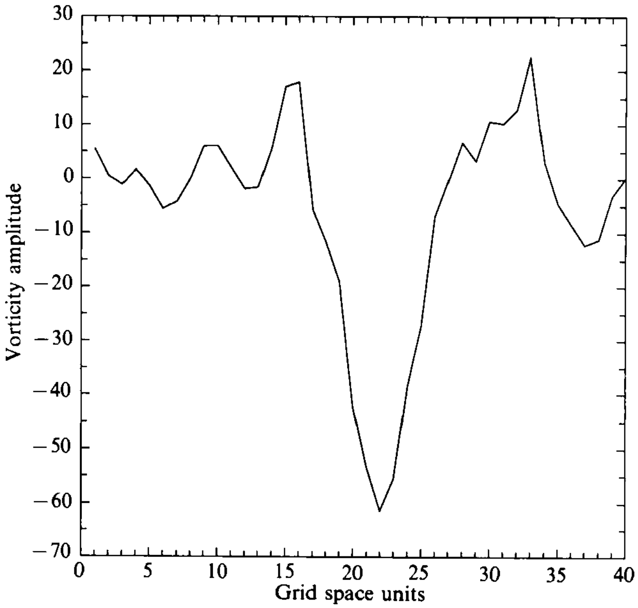

FIGURE 15. Cut through a typical vorticity tube along a direction perpendicular to its axis.

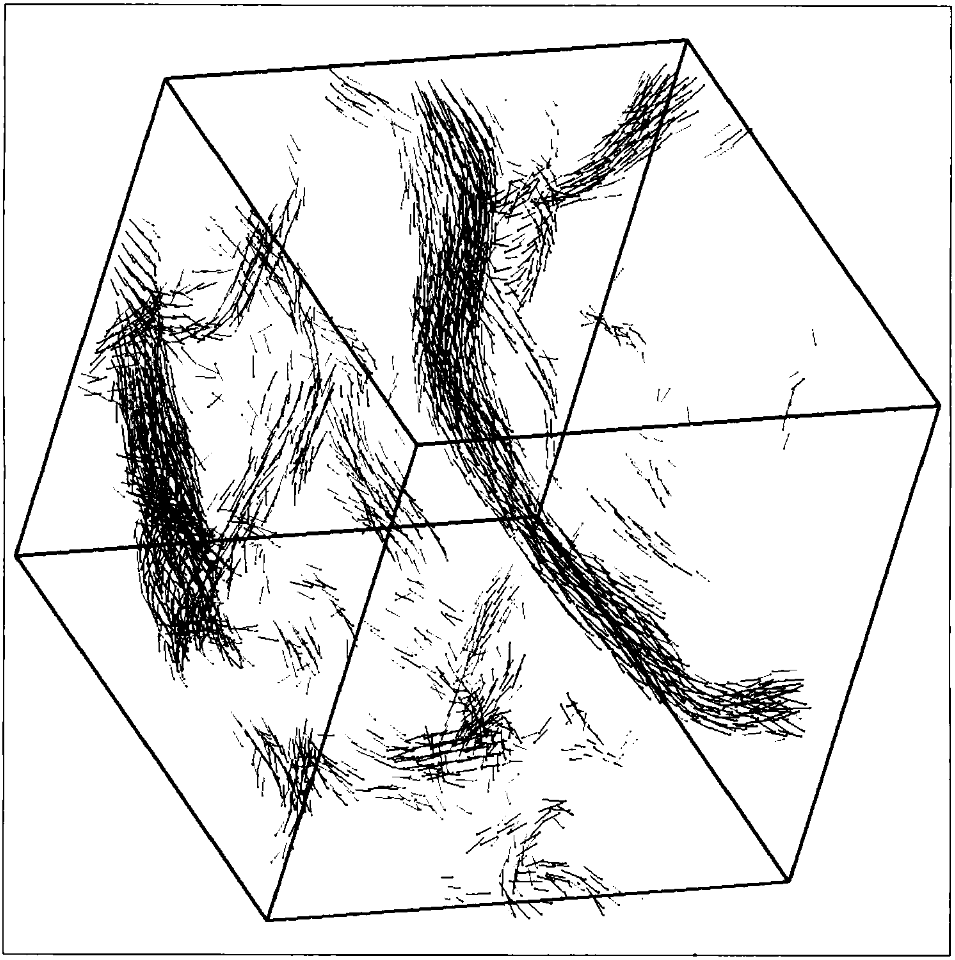

FIGURE 16. Detail of the vorticity field, showing a sub-cube of size one sixth of the complete cube, i.e. 40 grid points in each direction.

plots for the velocity field show mainly the forcing field if one uses a high threshold. But when the highest velocities are eliminated, the tubes are clearly visible.

From these visualizations, one is lead to the conclusion that these vorticity tubes, which seem to be the basic structure of three-dimensional homogeneous turbulence, involve all the scales of the flow. We have made the same kind of picture of the vorticity field after removing all dissipation-range scales. A smooth filter is applied in Fourier space in order to avoid spurious fluctuations. The large scales to which the forcing is applied were also removed. Figure 17 shows the same sub-cube as figure 16 when only inertial-range scales are left. One can see the external regions of the tubes. Some helical structure can be seen, as noted by She *et al.* (1990).

We have examined the shape of many of these tubes in order to see whether they are in fact rolled-up vorticity sheets, as suggested by Lundgren (1982), but this does not seem to be the case. Figure 18 gives an example of the projection of the velocity field on a plane perpendicular to a vorticity tube, while figure 19 shows the curves of constant vorticity on such a plane. As one can see from these figures, there is little evidence of spiral structure, or any other two-dimensional structure. A turbulence

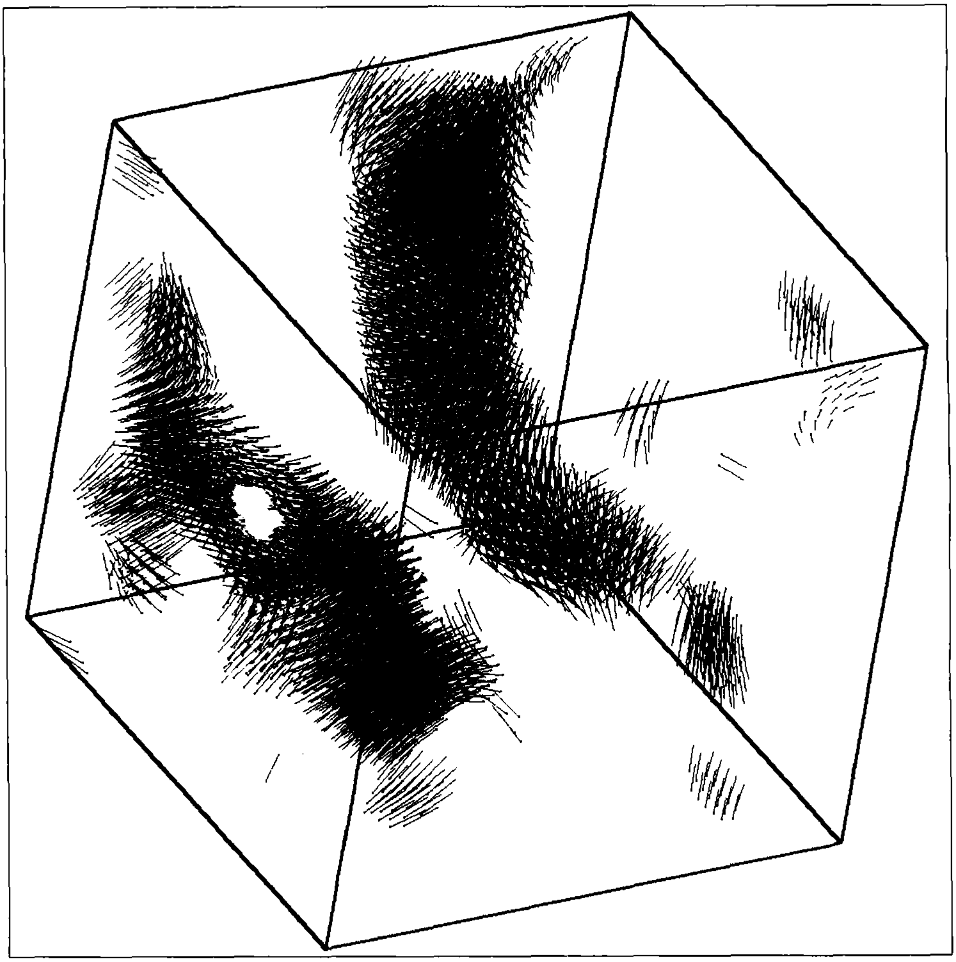

FIGURE 17. Same vorticity tube as in figure 6, but showing only inertial-subrange scales. Dissipation and energy-injection scales have been removed by filtering in Fourier space.

model based on a collection of vorticity tubes is presented in Tennekes (1968). This model predicts a $\partial_x v_x$ skewness S_3 independent of R_λ, which is what is found in numerical simulations (see above, §4), but also a flatness $S_4 \sim R_\lambda$, contrary to the result by Kerr (1985) and ourselves, which gives $S_4 \sim R_\lambda^{0.18}$.

Space correlations between vorticity and rate of strain were reported by Kerr (1985). At each grid point, we compute the eigenvalues $\lambda_1, \lambda_2, \lambda_3$ of the rate-of-strain tensor $S_{ij} = \frac{1}{2}(\partial_i v_j + \partial_j v_i)$, with λ_1 always negative and λ_3 always positive ($\nabla \cdot \boldsymbol{v} = 0$ implies $\lambda_1 + \lambda_2 + \lambda_3 = 0$). The intermediate eigenvalue λ_2 is found to be positive in approximately two thirds of the cases, in agreement with the results of the analysis of Kerr (1985) and Ashurst *et al.* (1987). Three-dimensional plots of the eigenvector fields, are used to study the correlations with vorticity. Let us call the eigenvectors associated with $\lambda_1, \lambda_2, \lambda_3$ respectively $\boldsymbol{e}_1, \boldsymbol{e}_2, \boldsymbol{e}_3$, each eigenvector being given the amplitude and sign of its associated eigenvalue. Figure 20 (plate 1) shows the field $\boldsymbol{e}_3$ (in red) together with the vorticity field (in blue). Again, only vectors above a certain amplitude threshold are displayed, and therefore the two fields are not generally shown at the same grid points. The highest rate of strain is seen to be generally in

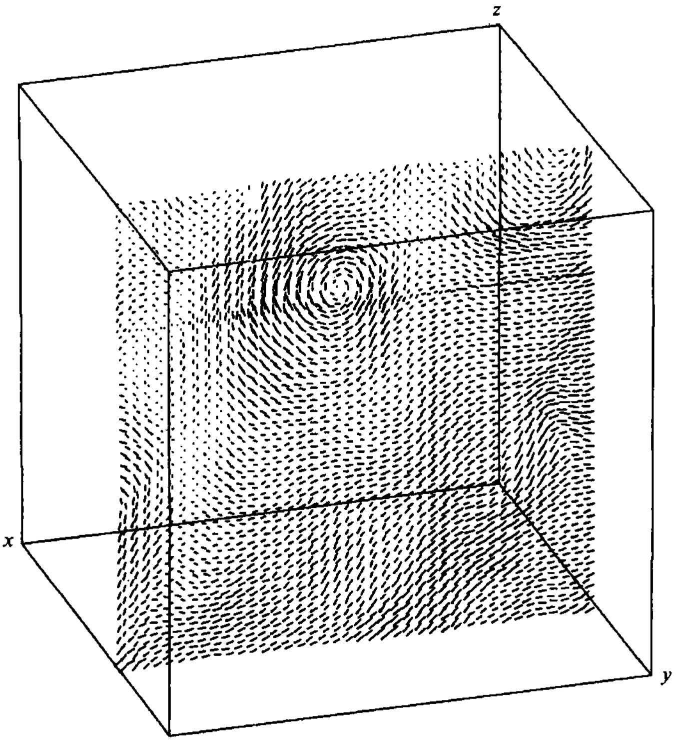

FIGURE 18. Projection of the velocity field on a plane perpendicular to a particular vorticity tube.

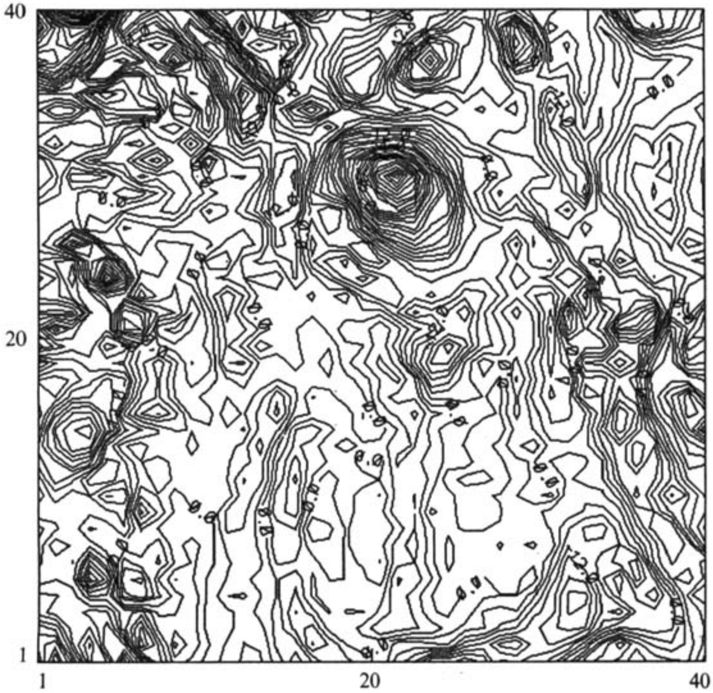

FIGURE 19. Curves of constant vorticity in a plane perpendicular to a selected vorticity tube.

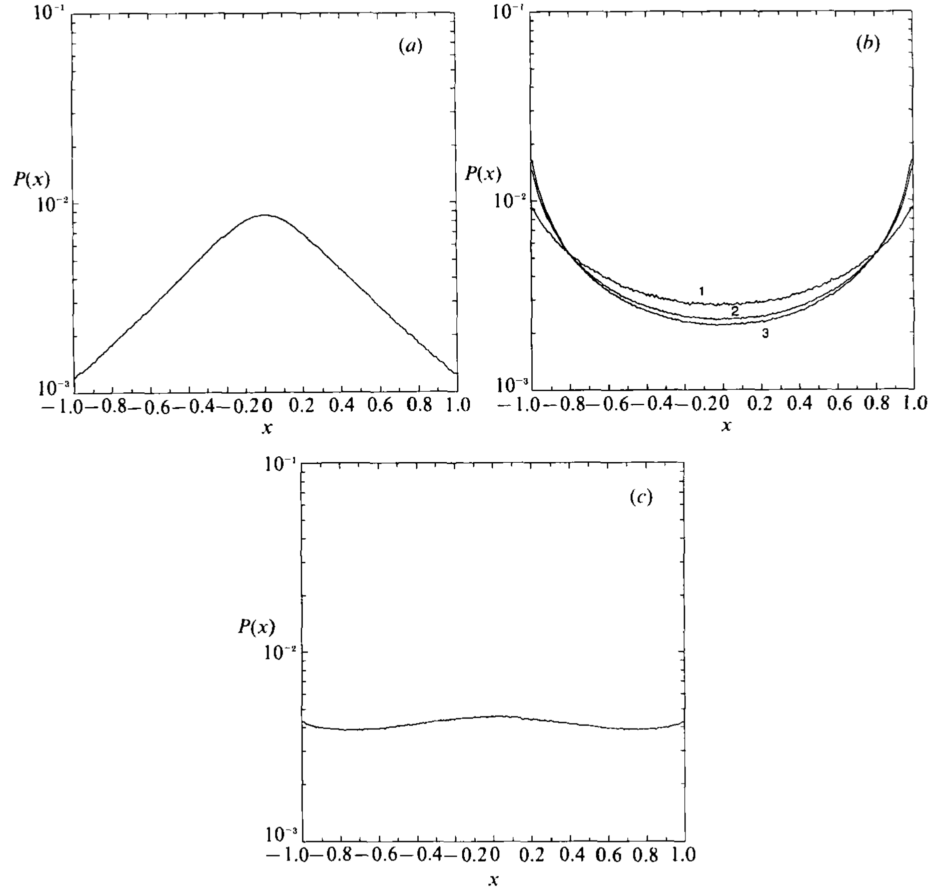

FIGURE 23. Distribution of the angle between the vorticity field and the rate of strain eigenvectors: (*a*) eigenvector e_1, associated with the smallest eigenvalue λ_1 (always negative); (*b*) eigenvector e_2, associated with the intermediate eigenvalue λ_2 (curve 1 for $\lambda_2 < 0$, curve 2 for all λ_2 values, curve 3 for $\lambda_2 > 0$); (*c*) eigenvector e_3, associated with the largest eigenvalue λ_3 (always positive).

the vicinity of vorticity tubes. The eigenvector e_3, associated with the positive eigenvalue, i.e. the stretching direction, is perpendicular to the vorticity. Note on the upper right of the picture, a vorticity tube seen along its axis, and on the left some tubes seen from the side, and the perpendicular field e_3 in their vicinity. Figure 21 (plate 1) is analogous to figure 20 but for e_1, the eigenvector associated with the negative eigenvalue of the strain, which is also seen to be perpendicular to the vorticity. The same tubes as before are seen, with the field e_1 perpendicular to them. Figure 22 (plate 2) shows again the same view of the vorticity, with this time the intermediate eigenvector e_2. This eigenvector is the one which is generally aligned with vorticity. It is difficult to see this for the previously mentioned vorticity tube seen along its axis, but it is clear for the tubes seen from the side. No clipping was available on the program used to produce these pictures, and this makes them a little confusing, owing to the excess of vectors in the background. Our conclusions are drawn from a fully three-dimensional examination of the flow using rotation. We could not find an example of e_3 aligned with vorticity. Note however that, up to now, our study has been biased towards high-vorticity regions. Different correlations might be seen when one examines low-vorticity structures.

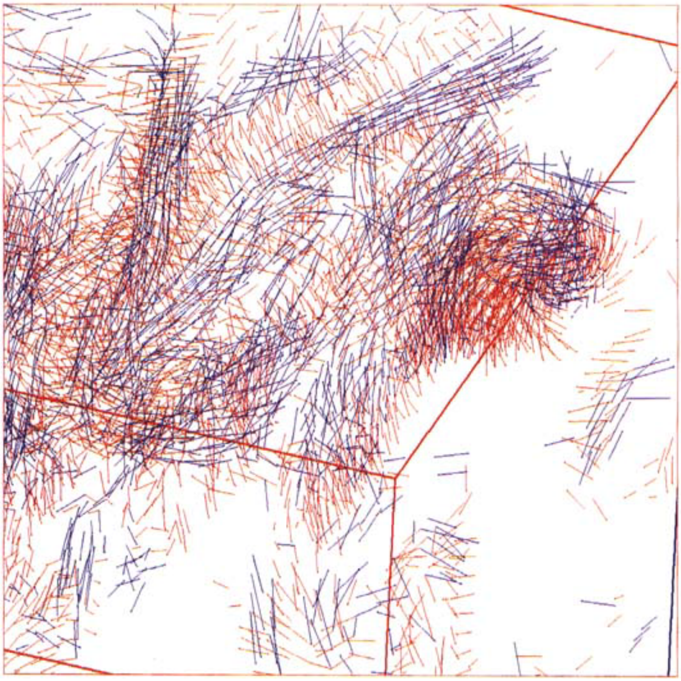

FIGURE 20. Vorticity field, in blue, and eigenvector e_3 associated with the largest (positive) eigenvalue, in red. Note in the upper right part of the figure the vorticity tube seen along its axis.

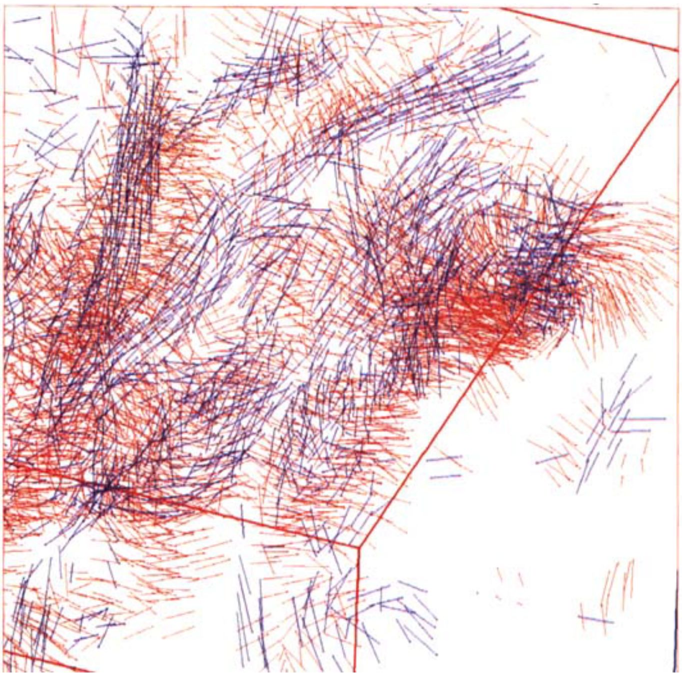

FIGURE 21. Vorticity field, in blue, and eigenvector e_1 associated with the smallest (negative) eigenvalue, in red. Note in the upper right part of the figure the same vorticity tube as in figure 12.

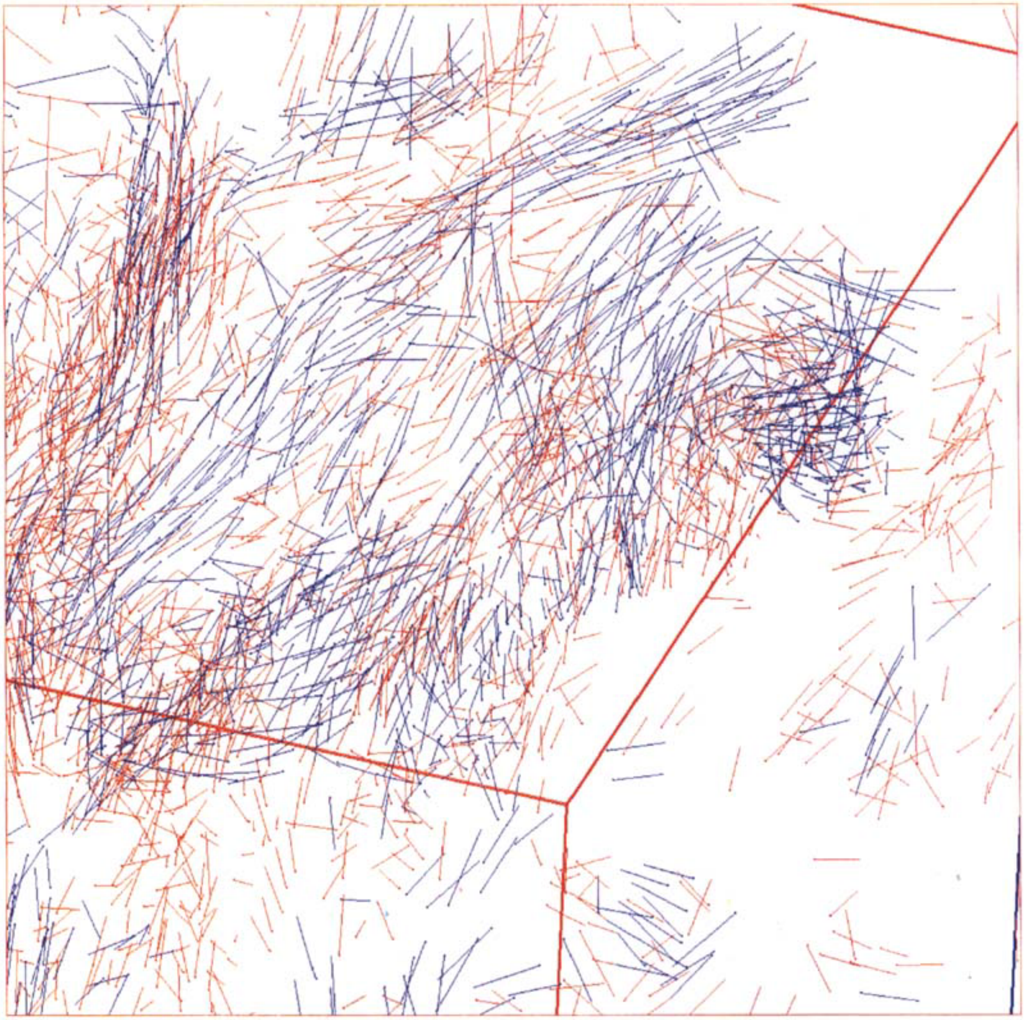

FIGURE 22. Vorticity field, in blue, and eigenvector $\boldsymbol{e}_2$ associated with the intermediate eigenvalue, in red.

A more quantitative picture of the alignment between the strain eigenvectors and vorticity is given by the distribution of the cosine of the angles between $\boldsymbol{\omega}$ and $\boldsymbol{e}_1$, $\boldsymbol{e}_2, \boldsymbol{e}_3$, shown in figure 23. In the case of $\boldsymbol{e}_2$, we give separately the distribution for $\lambda_2 < 0$ (curve 1), $\lambda_2 > 0$ (curve 3), and the complete distribution (curve 2). We find $\lambda_2 > 0$ in 75% of the cases. Our figure 23 is strikingly similar to figure 10 of Tsinober, Kit & Dracos (1991), obtained from experimental data.

The general alignment of vorticity with $\boldsymbol{e}_2$ reflects the quasi-two-dimensionality of the vortex tubes. Indeed, in two dimensions, $\lambda_2 = 0$, $\lambda_3 = -\lambda_1$ and $\boldsymbol{\omega}$ would be perpendicular to the plane $(\boldsymbol{e}_1, \boldsymbol{e}_3)$. A discussion of this correlation of vorticity with the intermediate rate-of-strain direction is presented in Ashurst *et al.* (1987), where an explanation is proposed using a model due to Vieillefosse (1982, 1984). According to calculations using this model, a vorticity tube is created along the direction of maximum stretching $\boldsymbol{e}_3$, but very soon becomes aligned with $\boldsymbol{e}_2$. We are presently trying to verify this explanation by following a vorticity tube back in time until the time of its formation. Our preliminary impression is that the tubes are generated by an instability of the Kelvin–Helmholtz type. If this is the case, the above picture would not be correct. The results of this investigation will be presented in a forthcoming paper.

6. Conclusion

We have obtained a turbulent homogeneous flow at $R_\lambda \approx 150$ and an inertial subrange more extended than in previous tri-dimensional simulations. The statistics of the velocity derivatives are strongly non-Gaussian both in the inertial and the viscous subranges. The distributions of velocity derivatives are more intermittent (i.e. have larger wings) than an exponential distribution. For the inertial-subrange scales, the distributions of velocity differences we obtain are consistent with distributions having exponential wings. The intermittency exponent μ is found to be 0.25. The log-normal and β-models of intermittency do not predict the nth-order structure-function scaling with n which we find. In addition, the Kolmogorov hypothesis of log-normality of the energy dissipation fluctuations is not confirmed by our calculations.

In physical space, we confirm the discovery by Siggia (1981) that the vorticity is organized in thin tubes. We find that the thickness of these tubes is intermediate between the dissipation scale and the Taylor microscale, while their length is comparable with the integral scale of the flow. Therefore, the picture of intermittency that emerges in physical space from our simulations is that all the scales present in the flow are correlated through these elongated structures. We confirm the results by Kerr (1985) that the vorticity is generally aligned with the strain eigenvector corresponding to the intermediate eigenvalue. But the precise determination of the mechanism by which these vorticity tubes are generated and their detailed dynamical evolution requires further study.

We are indebted to R. Kerr, J. Herring, Z. S. She, E. Jackson, S. A. Orszag, M. E. Brachet, P. L. Sulem, U. Schumann, M. Nelkin, M. E. McIntyre and A. Tsinober for numerous suggestions and discussions. The calculations presented were done on the Cray-2 of CCVR (Centre de Calcul Vectoriel pour la Recherche), Palaiseau, France. The main routine used in all our calculations is the Fast Fourier Transform of the Cray-2 library, which is a C. Temperton FFT adapted for this machine by Cray-Research. The NCAR graphics software has been used extensively.

REFERENCES

ANSELMET, F., GAGNE, Y., HOPFINGER, E. J. & ANTONIA, R. A. 1984 *J. Fluid Mech.* **140**, 63.

ASHURST, W. T., KERSTEIN, A. R., KERR, R. M. & GIBSON, C. H. 1987 *Phys. Fluids* **30**, 2343.

BACRY, E., ARNEODO, A., FRISCH, U., GAGNE, Y. & HOPFINGER, E. 1990 In *Turbulence and Coherent Structures* (ed. M. Lesieur & O. Metais). Kluwer.

BASDEVANT, C., LEGRAS, B., SADOURNY, R. & BELAND, M. 1981 *J. Atmos. Sci.* **38**, 2305.

BENZI, R., PATARNELLO, S. & SANTANGELO, P. 1987 *Europhys. Lett.* **3**, 811.

BRACHET, M. E., MEIRON, D. I., ORSZAG, S. A., NICKEL, B. G., MORF, R. H. & FRISCH, U. 1983 *J. Fluid Mech.* **130**, 411.

BRACHET, M. E., MENEGUZZI, M., POLITANO, H. & SULEM, P. L. 1988 *J. Fluid Mech.* **94**, 333.

CASTAING, B., GAGNE, Y. & HOPFINGER, E. J. 1990 *Physica* D **46**, 177.

CURRY, J. H., HERRING, J. R., LONCARIC, J. & ORSZAG, S. A. 1984 *J. Fluid Mech.* **147**, 1.

FRISCH, U., SULEM, P. L. & NELKIN, M. 1978 *J. Fluid Mech.* **87**, 719.

GOTTLIEB, D. & ORSZAG, S. A. 1977 *Numerical Analysis of Spectral Methods.* SIAM CBMS-NSF Regional Conference Series in Applied Maths.

HERRING, J. R. & MCWILLIAMS, J. C. 1985 *J. Fluid Mech.* **153**, 229.

KERR, R. 1985 *J. Fluid Mech.* **153**, 31.

KERR, R. 1990 *J. Fluid Mech.* **211**, 309.

KOLMOGOROV, A. N. 1941 *CR Acad. Sci. URSS* **30**, 301.

KOLMOGOROV, A. N. 1962 *J. Fluid Mech.* **13**, 82.

KRAICHNAN, R. H. 1974 *J. Fluid Mech.* **62**, 305.

KRAICHNAN, R. H. 1990 *Phys. Rev. Lett.* **65**, 575.

LEGRAS, B., SANTANGELO, P. & BENZI, R. 1988 *Europhys. Lett.* **5**, 37.

LUNDGREN, T. S. 1982 *Phys. Fluids* **25**, 2193.

MCWILLIAMS, J. C. 1984 *J. Fluid Mech.* **146**, 21.

MONIN, A. S. & YAGLOM, A. M. 1975 *Statistical Fluid Mechanics*, Vol. 2. MIT Press.

NELKIN, M. 1981 *Phys. Fluids* **24**, 556.

NOVIKOV, E. A. & STEWART, R. W. 1964 *Isv. Akad. Nauk SSSR Geophys.* **3**, 408.

OBOUKHOV, A. M. 1962 *J. Fluid Mech.* **13**, 77.

ORSZAG, S. A. 1972 *Stud. Appl. Maths* **51**, 253.

ORSZAG, S. A. & PATTERSON, G. S. 1972 *Phys. Rev. Lett.* **28**, 76.

PARISI, G. & FRISCH, U. 1984 In *Turbulence and Predictability, Varenna Summer School* (ed. M. Ghol, R. Benzi & G. Parisi), p. 84. North Holland.

PATTERSON, G. S. & ORSZAG, S. A. 1971 *Phys. Fluids* **14**, 2538.

SCHUMANN, U. & PATTERSON, G. S. 1978 *J. Fluid Mech.* **88**, 685.

SHE, Z. S., JACKSON, E. & ORSZAG, S. A. 1988 *J. Sci. Comput.* **3**, 407.

SHE, Z. S., JACKSON, E. & ORSZAG, S. A. 1990 *Nature* **344**, 226.

SIGGIA, E. D. 1981 *J. Fluid Mech.* **107**, 375.

SIGGIA, E. D. & PATTERSON, G. S. 1978 *J. Fluid Mech.* **86**, 567.

TENNEKES, H. 1968 *Phys. Fluids* **11**, 669.

TSINOBER, A., KIT, E. & DRACOS, T. 1991 *J. Fluid Mech.* (submitted).

VAN ATTA, C. W. & CHEN, W. Y. 1970 *J. Fluid Mech.* **44**, 145.

VIEILLEFOSSE, P. 1982 *J. Phys. Paris* **43**, 837.

VIEILLEFOSSE, P. 1984 *Physica* **125A**, 150.

YAMAMOTO, K. & HOSOKAWA, I. 1988 *J. Phys. Soc. Japan* **57**, 1532.